NOISE ESTIMATION OF AN ELECTRIC MACHINE FOR A PARALLEL HYBRID HELICOPTER PROPULSION SYSTEM

Sebastian Hakansson
German Aerospace Center
Cottbus, Germany

ABSTRACT

With the growing interest in electrifying the propulsion systems of current and future aircraft, research on the noise emissions of these new concepts is increasingly important. This is particularly true for future rotorcraft concepts, where the propulsion system and major noise sources are in close proximity to passengers. In this paper, the radiated noise of an electric machine that provides power to a parallel hybrid helicopter propulsion system during specific flight phases using various simulation software is estimated. To achieve this, a mission profile for an EC145 intended for Helicopter Emergency Medical Services is provided to calculate the power requirements of the machine. Using a simplified approach, the equivalent radiated power is calculated and then compared to the radiated sound obtained with a higher-fidelity model. The results indicate that the noise generated by electric machines in an aviation context is a significant noise source that should be taken into consideration during machine design.

INTRODUCTION

The aviation sector is currently experiencing a strong trend towards the electrification of propulsion systems. The aim is to reduce or eliminate harmful exhaust emissions, reduce noise and vibration, and explore new approaches to mobility in aviation. This development can be observed in both fixed-wing aircraft and rotorcraft. The latter case becomes obvious when considering the large number of concepts for electric vertical take-off and landing aircraft (eVTOLs). The electrification of larger helicopters is also receiving more attention.

The possibility of electrifying helicopters has been discussed in a number of studies, and further research is expected. A hybrid-electric system for an Eurocopter EC135 using diesel generators was studied by Jänker *et al.* (Ref. 1). For the electric machines, the authors considered transversal flux machines (TFM) with a very high torque density of 120 Nm/kg. They also cited the advantage of more flexible positioning of the powertrain components in the helicopter. Taking these results into account, a ring-type direct-drive flux switching permanent magnet machine (FSPM) with a Halbach array was designed by Sanabria-Walter (Ref. 2). It had a high torque-to-weight ratio of about 160 Nm/kg and a power-to-weight ratio of 6 kW/kg, and featured a novel air gap control mechanism with low-friction air bearings. In another study, Mercier and Gazzino analysed the current state of helicopter electrification based on state-of-the-art technologies and evaluated different powertrain architectures (Ref. 3). They also analysed the suitability and feasibility of these machines for different flight conditions. In addition, concepts for the electrification of an EC135 and H135 using fuel cells were investigated (Refs. 4–6). In these studies, the authors emphasised the high power requirements of electric machines, as well as the high weight and volume of batteries as energy storage devices in fully electric drives, i.e., in architectures that are intended to operate completely without internal combustion engines (ICE).

Most concept studies on the electrification of helicopters and aerospace propulsion systems in general focus on the topologies and architectures to be used, the resulting performance, and the mission profiles that can be achieved by using electric drives. However, electric machines also generate disturbing noise, which can often be masked by the presence of ICE (Ref. 7). With increasing electrification, these noise sources will play a more important role and therefore need to be considered early in the design process. Ideally, there will be a coupling between propeller design and electric machine design (Ref. 8).

The aim of this work is to design an electric machine for a light twin-engine multi-purpose helicopter in order to estimate its radiated noise level. An electric machine, including the necessary power electronics, is provided for each gas turbine to support it in certain flight phases. A battery is used as the energy source. The two identical machines are pre-dimensioned using an open-source pre-design tool, and their performance is simulated using a commercial multiphysics simulation software. Initial results for the acoustic sound power level of a single machine are determined and discussed. This work is intended to serve as a preparation for subsequent

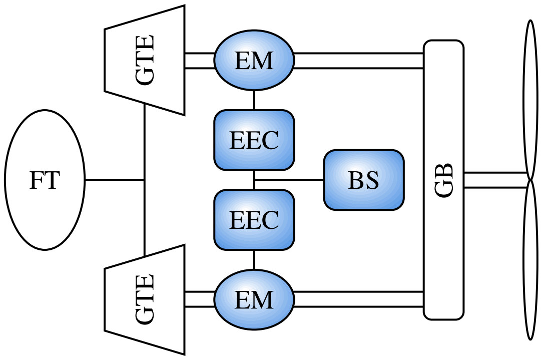

Figure 1. Schematic of the investigated parallel hybrid power train, with one supplementary electric machine per gas turbine. The power train consists of a fuel tank (FT), gas turbine engines (GTE), electric machines (EM), a gearbox (GB), electric energy converters (EEC), a battery (BS) and a propeller.

optimisations of electric machines suitable for aviation, with regard to increasing the power-to-weight ratio and improving efficiency, as well as investigating noise generation and corresponding noise reduction measures in the context of electrified powertrains in helicopters.

PROPULSION SYSTEM DESIGN

The electric machines are intended for a parallel hybrid drive for an EC145 (BK 117 C-2) to be used in Helicopter Emergency Medical Services (HEMS), as utilised by the German Air Rescue of the Allgemeiner Deutscher Automobil-Club e. V. (ADAC). Several missions per day may be flown, possibly with a short range, thus providing the option to recharge the batteries on the ground between assignments.

An initial concept for a powertrain architecture was developed. Each of the two installed gas turbines is supplemented by a 320 kW peak, 236 kW continuous electric machine, whose power will be applied to the gas turbine shaft. The electric part of the power train provides 50% of the power required during periods of high power demand, such as vertical flight and climb in forward flight. The two gas turbines could then theoretically be downsized, saving weight and volume, or operated closer to their design point to optimise fuel consumption. A battery is planned to provide the necessary energy. Figure 1 shows a schematic of the powertrain architecture.

The architecture consists of the conventional power train components, including a fuel tank (FT), gas turbine engines (GTE), gearbox (GB), and propeller, as shown by Bolvashenkov *et al.* (Ref. 9). For the electrical part of the parallel hybrid power train, two electric machines (EM), electric energy converters (EEC), and a battery (BS) are introduced. The electric machines are placed on the shaft of the respective gas turbine engine, so that some installation space must be taken into account. They provide power to the gas turbine shafts as required or in emergency situations (i.e. one engine inoperative, OEI). At the same time, the electric machine can be used in generator mode to recharge the battery in certain flight phases, as discussed by Donateo *et al.* (Ref. 10).

Table 1. Mission profile point identifier (pid) and respective flight phase.

pid	Flight phase	pid	Flight phase
0	vertical climb	8	climb in fwd. flight
1	climb in fwd. flight	9	fwd. flight
2	fwd. flight	10	climb in fwd. flight
3	climb in fwd. flight	11	fwd. flight
4	fwd. flight	12	descent
5	climb in fwd. flight	13	vertical climb
6	descent	14	descent
7	landing / end	15	landing / end

The electric powertrain significantly reduces the maximum payload, mainly because of the weight of the battery. As the electric powertrain is primarily intended to provide assistance during periods of high power demand, the battery can be smaller overall. There may be downtime between missions. During these periods, the battery could be recharged on the ground.

Mission profile

A corresponding mission profile of a German air rescue helicopter (DRF) is shown in Figure 2. It was created from an individual flight log of one helicopter, which was accessed from a flight tracking company that displays aircraft and flight information in real-time (Ref. 11). Contrary to the current investigation, an EC145 T3 was tracked, but this should not play a decisive role in the creation of a representative Emergency Medical Services (EMS) mission profile.

The profile shows the altitude of the vehicle over time for a 15-minute flight from Mannheim-City Airport (ICAO: EDFM) heading approximately 60 km south-east. A 30-minute downtime with no Automatic Dependent Surveillance Broadcast (ADS-B) signal suggests an EMS operation at an altitude of 400 m above sea level, with another 15-minute return flight, possibly to a hospital in the vicinity of Heidelberg.

The profile was edited in order to obtain distinct flight phases and to ease the subsequent power calculation. This means that data points with missing entries were omitted, the altitude at the mission end was adopted from the mission start, and the vertical speed was manually calculated as a mean value to reach the next point. The phases are labelled with a profile point identifier (pid), starting from 0 to 15. Table 1 gives an overview of all flight phases of the edited mission profile.

Power estimation

In order to calculate the required power for the helicopter and thus the power that has to be provided by the electric machines, the mission profile was subdivided into a number of

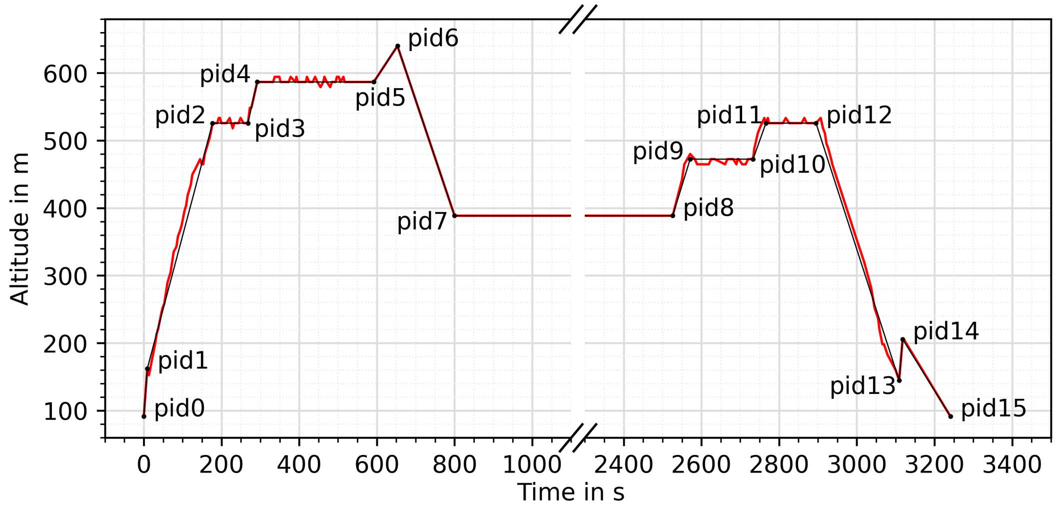

Figure 2. Mission profile of an individual helicopter of the German air rescue (DRF) from August 2024, showing the vehicle's altitude over time. Actual ADS-B data is shown in red, with the cleaned and edited profile in black. See Table 1 for reference.

different flight phases. The four different phases are: (1) vertical climb, (2) climb in forward flight, (3) forward flight and (4) descent. In the following section, methods are presented to estimate the power for each state.

The investigated vehicle, an EC145 (BK 117 C-2), has a main rotor with four blades and a rotor diameter D of 11 m with an approximate blade chord length l_c of 0.325 m. The tip speed of the rotor V_{tip} is set to a constant value of 220.8 m/s.

Because the main task of this study is to investigate the noise of the supporting electric machines for the hybrid powertrain, the weight of the vehicle was set to a constant value, i.e. its maximum allowed value of 3,585 kg. By doing so, enough payload mass is available to include the components of the electrical part of the powertrain. Thus, the subsequent power estimation is not an iterative task, and the resulting mass of the electric machines, as well as an estimation for the necessary electric energy converters and the battery, has to be made only once. The power estimation does not consider a change of mass due to burning fuel.

The following power estimation is based on a simplified blade element theory, thoroughly covered in a book by Seddon and Newman (Ref. 12). The required thrust T corresponds to the weight force, i.e. the take-off mass multiplied by the acceleration due to gravity g. For the EC145 with a maximum take-off weight (MTOW) of 3,585 kg, 35.2 kN of thrust is therefore required.

Vertical Climb The power necessary to perform a vertical climb is given by Eq. (1) as

$$P = \kappa \left(V_c + v_i\right) T + \frac{1}{8} C_{D_0} \rho \sigma A V_{tip}^3, \tag{1}$$

where V_c is the vertical or climb speed of the aircraft, v_i is the induced velocity, ρ is the air density at the specific flight level, σ is the solidity factor, and A is the area of the main rotor disc. κ is an empirical constant to account for non-uniform inflow as well as tip losses. Seddon and Newman (Ref. 12) suggest a value of 1.15 for vertical climb. C_{D_0} is the averaged airfoil or blade profile drag coefficient. In this simplified approach, it is set to a constant across the blade. Following Seddon and Newman, a typical value is 0.01. The combined climb and induced speed in Eq. (1) is given by

$$V_c + v_i = \frac{1}{2} V_c + \sqrt{\left(\frac{1}{2} V_c\right)^2 + \frac{T}{2\rho A}}, \tag{2}$$

whereas the solidity factor σ is given by

$$\sigma = \frac{N_b l_c}{\pi R}. \tag{3}$$

Here, N_b is the number of blades on the rotor, and R is the rotor radius.

Climb in forward flight The power coefficient C_P for a forward flight and climb phase is given by Eq. (4) as

$$C_P = \kappa \lambda_i C_T + \frac{1}{8} \sigma C_{D_0} \left(1 + k\mu^2\right) + \frac{1}{2} \mu^3 \frac{A_{efp}}{A} + \varepsilon \lambda_c C_T. \tag{4}$$

Here, λ_i is the ratio of the induced velocity in forward flight $v_{i_{fwd}}$ to the rotor tip speed, μ is the ratio of forward flight speed V_{fwd} to the rotor tip speed, λ_c is the ratio of climb speed V_c to the rotor tip speed, and k is another empirical correction factor to give more reasonable results when considering profile drag. A value of 4.65 is recommended by Seddon and Newman (Ref. 12). A_{efp} is the equivalent flat plate area, set to a value of 0.016 times the rotor area. ε is a factor that "takes into account additional losses caused by the changes of relative flow direction in climb" (Ref. 13). For the calculations performed in this study, ε was set to 1. For a forward flight and climb phase, a value of 1.2 should be used for κ according to Seddon and Newman. C_T in the first and last term of Eq. (4) is the thrust coefficient, which is given by

$$C_\mathrm{T} = \frac{T}{\rho A V_\mathrm{tip}^2}. \tag{5}$$

In order to calculate λ_i, the induced velocity in forward flight $v_{\mathrm{i_{fwd}}}$ is required. It can be calculated by

$$v_{\mathrm{i_{fwd}}}^2 = -\frac{1}{2}V_\mathrm{fwd}^2 + \frac{1}{2}\sqrt{V_\mathrm{fwd}^4 + 4\left(\frac{T}{2\rho A}\right)^2}. \tag{6}$$

Using the calculated power coefficient C_P from Eq. (4), the required power for the forward flight and climb phase can be calculated as

$$P = C_\mathrm{P}\rho A V_\mathrm{tip}^3. \tag{7}$$

Forward flight The power estimation for the forward flight condition is quite similar to the forward flight and climb phase. It can be calculated using

$$P = \kappa v_{\mathrm{i_{fwd}}} T + \frac{1}{8}\sigma C_{\mathrm{D_0}}\rho A V_\mathrm{tip}^3\left(1+k\mu^2\right) + \frac{1}{2}\rho V_\mathrm{fwd}^3 f. \tag{8}$$

Descent The required power for descent was calculated according to Eq. (4), using negative vertical speeds. All other parameters and coefficients were kept the same.

Results Using the aforementioned Eqs. (1) to (8), the total power for all flight phases of the mission profile was calculated. In order to account for the necessary tail rotor and accessories power, as well as transmission losses, the estimated power was increased by an additional 15%.

Figure 3 shows the results, together with the power that is provided by the electric machines. They are meant to support the gas turbines in the two flight phases "vertical climb" (pid 0 and 13) and "climb in forward flight" (pid 1, 3, 5, 8 and 10) with 50% of the requested power.

Mass breakdown

The empty weight of the helicopter is 1792 kg, so 1793 kg of useful load are available. For an EMS mission, a pilot and two HEMS crew are assumed, each weighing 80 kg. The patient weighs 80 kg and the Basic EMS Kit for the EC145 as well as additional required equipment, has a mass of 167.6 kg according to a technical data sheet for this specific vehicle (Ref. 14).

Two electric machines are planned to support the gas turbines. A single machine weighs approximately 66 kg, including the stator, rotor, magnets, windings, and impregnation, as well as a casing, shaft, and two bearings. For the electric energy converters that convert the DC voltage from the battery to the AC voltage required at the terminals of the electric machines, a gravimetric power density of 25 kW/kg was assumed based on the studies of Kugener *et al.* (Refs. 15, 16). A power rating of 350 kW (peak rating of the machine with a safety margin of approximately 10%) and a 3L-NPC topology was selected in this study. Using one 3L-NPC inverter for each electric machine, a total mass of 28 kg was estimated. For the DC/DC converter, which integrates the high voltage DC current from the battery into the high voltage (HV)-DC bus and allows for bidirectional power flow (e.g. charging the battery), a gravimetric power density of 20 kW/kg was assumed.

Table 2. Mass breakdown of all considered components.

	Mass in kg
Empty weight	1,792
Pilot	80
HEMS crew	2×80
Basic EMS kit	140.5
Add. req. equipment	27.1
Patient	80
electric machines	2×66
AC/DC Converter	2×14
DC/DC Converter	2×17.5
Battery	132.6
Fuel	694

Using the mission profile, the duration of each flight phase was determined and the electric energy required to operate the electric machines was calculated. Using power and energy-to-mass ratios, the mass of the battery can be roughly estimated. The electric motors are active in pid 0, 1, 3, 5, 8, 10, and 13. For the vertical climb with 9 seconds of flight phase duration, an energy of 2,260 Wh is necessary. For the climb in vertical flight phases, a total energy of 24,266 Wh has to be provided. Li-Ion batteries are planned as the energy source. Sahoo *et al.* (Ref. 17) gave an overview of current state-of-the-art as well as future projected specific energy densities for batteries and other energy storage technologies. A rather conservative specific energy density of 200 Wh/kg was used in this study. Therefore, the total mass of the battery is 132.6 kg. Table 2 gives an overview of all obtained masses.

Design of the electric machine

In order to design the machine, an open-source tool was used, taking into account the requirements for the torque to be provided at a given speed (Ref. 18). Inputs to the tool included the number of pole-pairs, the materials to be used, the maximum current density allowed in the winding, and the maximum saturation limits. The winding system can also be influenced, for example, by specifying the slot fill factor or the winding type. The tool calculates the geometric dimensions of the active part of the machine (stator lamination diameter,

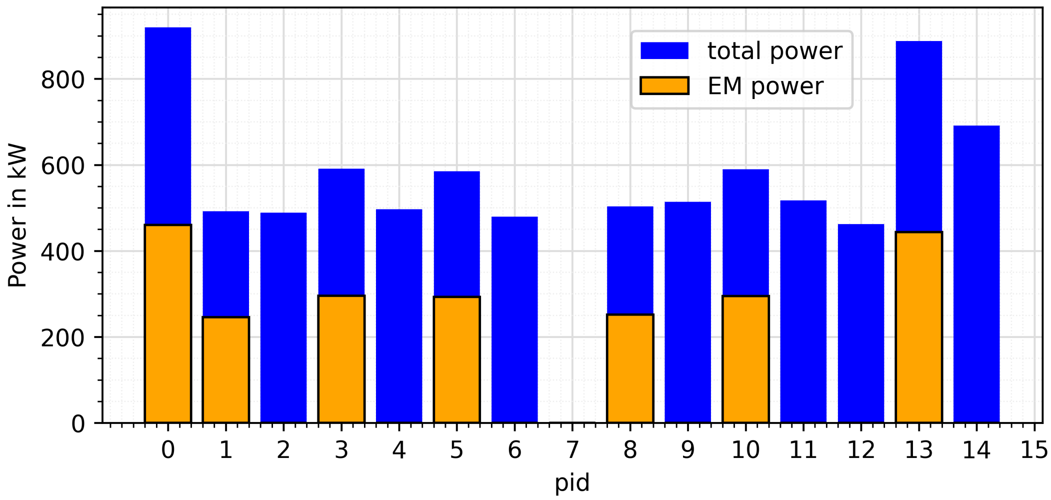

Figure 3. Power estimation for different flight phases of the helicopter and respective share of the electric power train. See Table 1 for reference.

slot dimensions, magnet thickness and height, etc.). It also determines and provides parameters of the electromagnetic system. These include, for example, the analytically determined inductances, resistances, induced voltage, and current to be applied.

The parameters determined in this way were used to model the machine in a commercial finite element software (EMag), which then provides accurate predictions in the fields of electromagnetic and electrical performance, coupled thermal behaviour, and mechanical strength. An interface was used, which feeds the data from the open-source tool directly into the simulation environment. From there, an initial design transformation took place, where the model was pushed towards a more realistic design (e.g., setup of a cooling system and integration of a sleeve holding the magnets in place, as well as the casing and bearings). From there, it was then analysed for its electromagnetic properties, and the resulting force density in the air gap, necessary for the noise estimation, could be determined.

Furthermore, an additional optimization process was performed. The mentioned open-source pre-design tool takes input parameters at rated speed, i.e., at the point of maximum torque and power. This results in a machine design that is capable of providing peak power, but only for a limited amount of time. In continuous operation mode, the temperatures inside the windings and the magnets will increase until they reach their respective maximum allowable rating. By using the requirements coming from the mission profile, a cooling system was designed in order to obtain a reasonable continuous power curve. By applying a multi-physics, multi-objective optimization, the characteristics of the initial design (e.g., machine weight, power, efficiency, phase current, ...) were further optimized, thus reaching a higher specific power rating. To this end, a number of parameters were determined, which were used to form a meta model of the machine in a commercial software. In a subsequent step, the parameters were varied, and optimal parameter configurations were obtained. A design was then chosen from a Pareto front and finally validated by performing simulations in a commercial software. The parameters that were varied included the stator and rotor lamination geometry, the tooth geometry, the magnet angle and thickness, the turns per coil, and the current density.

Final design

The final design is a radial flux permanent magnet synchronous machine (PMSM) in an in-runner configuration with surface-mount magnets (Ref. 19). The number of slots N is 24, and the number of pole-pairs p is 10. It has a rather large aspect ratio (i.e., ratio of stator lamination diameter to lamination length) of 3.16. A gearbox is not planned for the initial design, so the machine will deliver the torque at the same speed as the gas turbine shaft, i.e., 6,000 rpm. The machine has a three-phase, two-layer, concentrated winding system. Vacoflux 48 is used for both the stator and rotor laminations, and Recoma 35E is used for the samarium cobalt (SmCo) permanent magnets. The windings are made of copper, while the housing is made of aluminium alloy, and the shaft is made of of stainless steel. The machine is solely cooled by air, which is forced through the air gap between the stator and rotor, through the slots, and over the housing. In continuous operation, the magnets are far from their respective critical temperature, while the windings are operated in the vicinity of their limit of 160 °C. The temperatures in the windings are the reason why the optimizer favoured a design with a small axial extent and thus a large aspect ratio. A rotor banding is used to hold the magnets in place. The rotor yoke, which was also optimized with regard to lower mass, appears to be very small but is sufficiently dimensioned with regard to the magnetic flux and saturation levels. A very simplified casing, bearing,

Table 3. Overview of major specifications of the initial and the optimized, final machine design.

Parameter	Symbol	Initial	Optimized
number of slots	N	24	24
stator outer diameter (mm)	D_{so}	427.5	492.9
stator bore diameter (mm)	D_{si}	355.3	419.1
tooth width (mm)	w_{t}	23.9	25.9
slot depth (mm)	h_{s}	23.7	22.4
slot opening (mm)	b_{s}	4	3.4
rotor outer diameter (mm)	D_{ro}	336.8	394.8
rotor inner diameter (mm)	D_{ri}	310	377.3
lamination length (mm)	l	80.4	76
motor length (mm)	l_{m}	151.6	156
housing thickness (mm)	h_{h}	5	5
number of poles	$2p$	20	20
magnet thickness (mm)	h_{m}	7.6	9.5
magnet arc (EDeg)		123.5	160
air gap height (mm)	g	1.67	1
electric frequency (Hz)	f_{e}	1,000	1,000
phase advance (EDeg)		0	14.6
number of turns		4	4
RMS current density (A/mm^2)	J	9.65	6
stator phase peak current (A)	I_{p}	440	281.5
copper slot fill factor		0.45	0.45
lamination stacking factor		0.97	0.97
DC Bus Voltage (V)	V_{DC}	1,000	1,000

and shaft combination is used to house the active components of the electric machine. This casing acts as the radiation surface for the subsequent acoustic analysis. The specifications of the final machine design can be found in Table 3, and a schematic of the machine is shown in Figure 4.

The final design of the machine has a peak power output of 320 kW at 6,550 rpm, slightly above the design point. At a speed of 6,000 rpm and a peak phase current of 281.5 A, the machine is able to deliver 372 Nm of torque, equalling 236 kW continuous shaft power, see Figure 5. The efficiency at this operating point is close to 97%.

NUMERICAL PREDICTION OF NOISE

In order to produce torque, an electric machine needs to build up an electromagnetic field inside its active parts. In the case of a PMSM, this is a superposition of the two fields provided by the permanent magnets and the armature, respectively. By solving the model, one can obtain the magnetic flux densities B_{t} in radial and B_{r} in tangential direction. The first one is responsible for producing the torque, while the second one is the main source of electromagnetically induced noise. By using the flux densities, the force density in radial direction f_{r} can be computed as

$$f_{\mathrm{r}}(x,t) = \frac{1}{2\mu_0}\left[B_{\mathrm{r}}^2(x,t) - B_{\mathrm{t}}^2(x,t)\right], \tag{9}$$

while the component in the tangential direction f_{t} is obtained

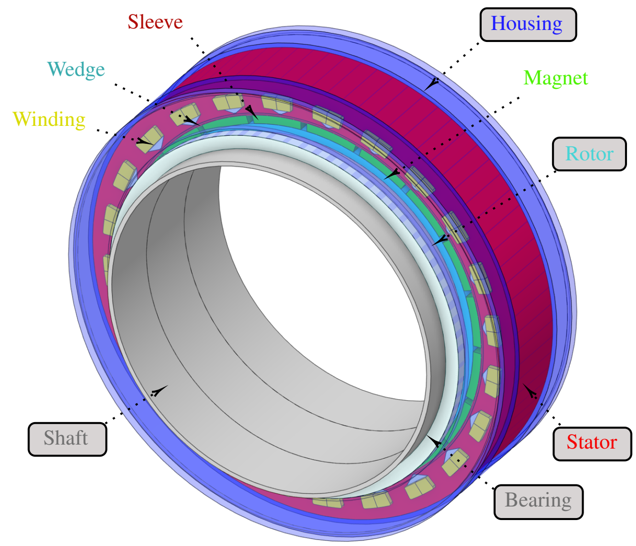

Figure 4. Schematic showing the final design of the machine, together with the present components. Components labelled with a box indicate their presence in the models used for subsequent noise estimation.

by

$$f_{\mathrm{t}}(x,t) = \frac{1}{\mu_0}\left[B_{\mathrm{r}}^2(x,t)B_{\mathrm{t}}^2(x,t)\right]. \tag{10}$$

Here, μ_0 is the magnetic permeability, x is the circumferential position inside the air gap, and t is time. With the force density, which can be understood as a magnetic pressure, the forces acting on the surface of the stator teeth facing the air gap can be calculated as

$$F_{\mathrm{r}} = f_{\mathrm{r}}(x,t)\, l_{\mathrm{arc}}\, l \tag{11}$$

and

$$F_{\mathrm{t}} = f_{\mathrm{t}}(x,t)\, l_{\mathrm{arc}}\, l. \tag{12}$$

where l is the lamination length and l_{arc} is the length of the stator tooth surface in circumferential direction. Following this approach, a force component in each direction acting in the centroid of the surface for each stator tooth is obtained. These electromagnetically induced forces are then used as excitation in the subsequent *harmonic response* analysis.

Modal analysis

In preparation for the *harmonic response* analysis, a modal analysis was performed. For this, the geometry of the machine was imported into a structural finite element analysis (FEA) software, and the eigenfrequencies as well as the eigenmodes were calculated. While the stator and rotor lamination, as well as a simplified housing, bearings, and shaft components, were considered, the windings, wedges (to hold the windings

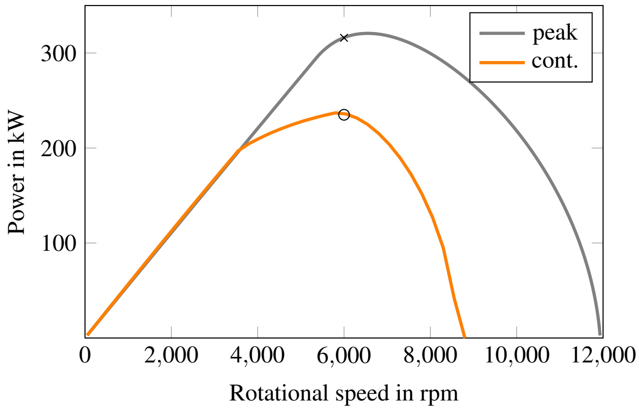

Figure 5. Peak and continuous power-speed-curve of the final machine design. Markers are showing peak (×) and continuous (○) power at 6,000 rpm.

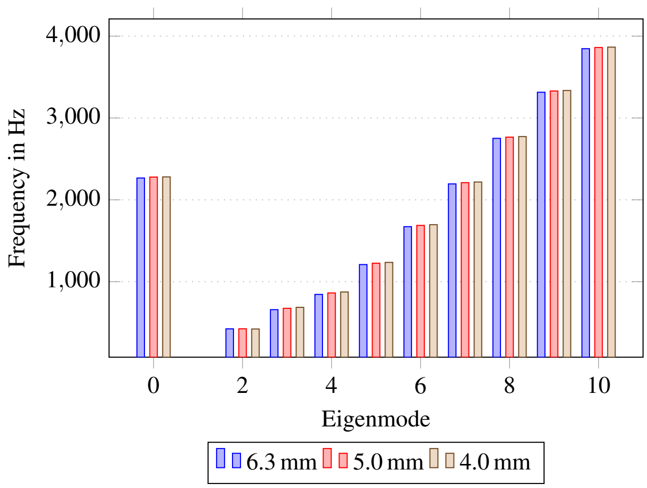

Figure 6. Results of the mesh sensitivity study showing the obtained natural frequencies from the modal analysis for the first couple of circumferential eigenmodes with three different element sizes.

in place), and magnets were omitted in order to reduce the element count of the mesh and thus lower the required computational time. To account for the mass of the windings, a so-called distributed mass element was applied to the inside of the stator slots, distributing the total mass of the windings of 4.29 kg equally to all slots. The same was done for the end-winding mass at the front and back of the stator lamination. The damping ratio was set to a fixed value of 5%.

A mesh with an approximate element size of 5 mm was used, leading to a total of 113k elements. The mesh was built upon tetrahedral and hexahedral elements. A small mesh sensitivity study was performed with half and double the element count, corresponding to an element size of 6.3 and 4 mm, respectively. The study showed only a minor effect of the element count on the obtained eigenfrequencies, with a lower element count leading to slightly lower frequencies, while a finer resolution led to slightly higher frequencies. Figure 6 shows the results of this study.

Harmonic response

In combination with the modal analysis of the stator, the forces derived from the electromagnetic analysis were applied to the individual stator teeth at their surface centroid as part of a *harmonic response* analysis, and the acoustic sound power level was determined. This model calculates the equivalent radiated power (ERP) based on the radial vibration velocity on the structural surface, being a function of the force wave amplitude at specific spatial and frequency orders, as well as the eigenmodes of the excited structure (Ref. 20). This is a simplified calculation of the sound power, which is based on plane wave propagation. Instead of the sound particle velocity, the normal velocity on the surface of the housing is used, assuming that they are equal. The ERP can be calculated as

$$P_{\mathrm{ERP}} = \frac{\rho c}{2} \int_A \hat{v}_{\mathrm{n}}^2 \, dA. \tag{13}$$

Here, c is the speed of sound, and $\hat{v}_{\mathrm{n}}$ is the amplitude of the normal velocity on the surface of the radiating structure, in this case, the housing. The ERP is simple to calculate but does not consider the shape of the radiating surface nor the wavelength of the sound. As a result of this, the radiated sound might be overestimated at lower frequencies, specifically for smaller machines. The true radiated acoustic power is given by

$$P = \sigma_{\mathrm{re}}(f) P_{\mathrm{ERP}}, \tag{14}$$

with σ_{re} being the radiation efficiency. This efficiency is a function of the sound frequency and takes values close to zero for low frequencies and otherwise values close to unity. This means that for low-frequency radiation, an overestimation of the radiated sound power is to be expected when the ERP is used to estimate the noise. The Helmholtz number He is a metric that relates the acoustic wavelength λ to a characteristic length in order to determine the acoustic behaviour. It can be used to decide whether a low or a high frequency radiation is present for the machine under investigation, thus determining the radiation efficiency. It is given by

$$He = \frac{2\pi}{\lambda} R_{\mathrm{h}}, \tag{15}$$

with λ being the acoustic wavelength and R_{h} the radius of the whole structure, here once more the casing or housing of the machine. A Helmholtz number below one indicates a low frequency, while a number of 10 or greater indicates a high frequency situation where overestimation of the ERP is unlikely to happen, as discussed by Kvist *et al.* (Ref. 21).

Figure 7 shows the current workflow used to obtain the ERP of the machine. It includes the design of the machine using the open-source tool (Ref. 18) as well as the optimization process using a commercial software, the electromagnetic calculation (here labelled as EMAG) to obtain the electromagnetic forces acting inside the air gap, the modal analysis, and the determination of the sound levels as part of the harmonic analysis on the basis of a mode superposition (MSUP).

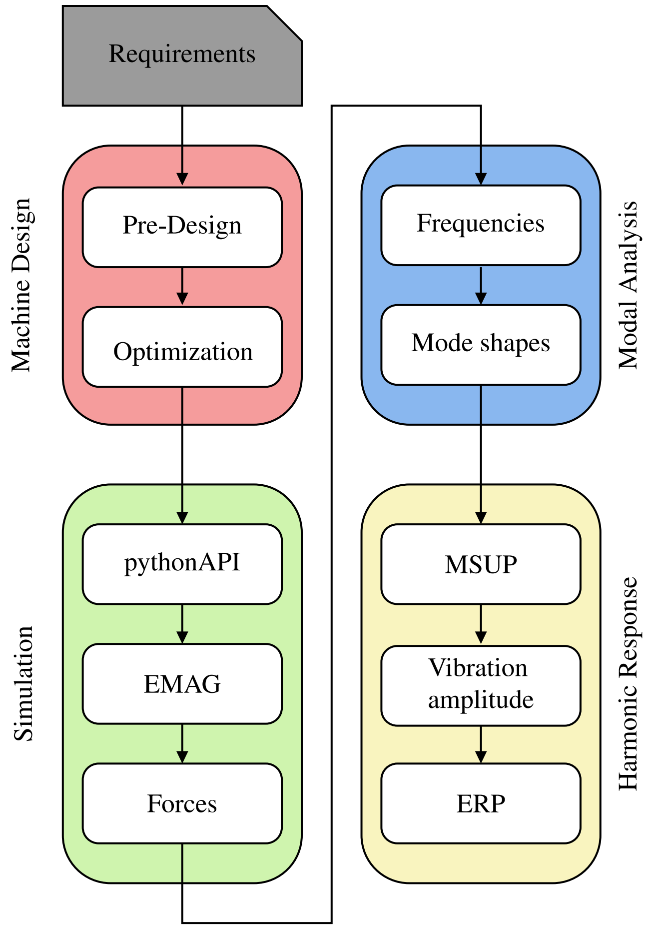

Figure 7. Overview of the current workflow to obtain the equivalent radiated power of the machine.

Harmonic acoustic

In addition to the *harmonic response*, a *harmonic acoustic* analysis was conducted. It takes the solution of the *harmonic response* as an input and applies the obtained amplitude of the surface vibration velocity onto a predefined fluid-structure-interaction surface. A sphere containing the fluid (e.g. air) was then used to provide a fluid region around the structure and the (true) sound power was solved for.

Similar to the structural domain, the surrounding fluid domain needs to be meshed. The radius of the sphere was chosen in such a way that a full wave of the longest acoustic wavelength of interest could be fitted in all three dimensions around the machine. The mesh element size was chosen to ensure that at least six elements were available to resolve the smallest acoustic wavelength present.

The difference between the largest and the lowest frequency can lead to a very large spectral gap and therefore to very small elements in a rather large sphere when the whole frequency range of up to 20 kHz is considered. This can lead to models with a very high element count and hence to excessive computational costs. To mitigate this effect, the frequency range was split into a number of frequency bands that were modelled and simulated independently, thus reducing the computational requirements and, in turn, the total time necessary to obtain a solution.

Table 4. Considered frequency bands for the *harmonic response* simulation. The *harmonic response* simulation was solved every 1,000 Hz in the respective band.

Band	Solution frequencies in Hz	Solution available
0	1,000–3,000	✓
1	4,000–8,000	✓
2	9,000–11,000	✓
3	12,000–14,000	✗
4	15,000–17,000	✗
5	18,000–20,000	✗

Table 4 gives an overview of the considered frequency bands. The frequency bands “3” to “5” were not solved in the current study because of limitations of the hardware used and due to the fact that the main contribution of noise is located at frequencies below 8,000 kHz. The reason for the hardware limitation is the very large outer diameter of the machine, while at the same time the axial dimension is shorter. The machine therefore has a “doughnut” shape. The radius of the buffer layer, whose extent or height was set to the largest wavelength to be resolved, was determined by the radius of the casing. As an example, for band “1” with a lower frequency limit of 4,000 Hz the largest wavelength is 85 mm. Together with the stator lamination diameter D_{so} of 492.9 mm and the housing thickness h_{h} of 5 mm, a sphere radius of 336.5 mm was used. The axial extent of the machine l_{m} is, however, only 156 mm. Therefore, three full waves of the largest wavelength to be resolved can be fitted in the front and in the back of the machine. As a consequence, the model has too many elements at these positions, which increases the size of the mesh.

The mesh used for frequency band “1” is shown in Figure 8. It consists of 3.1 million elements. The largest wavelength is 85 mm, while the smallest wavelength for a frequency of 8,000 Hz is 42.5 mm. With six elements per wavelength, the element size is therefore approximately 7 mm.

RESULTS AND DISCUSSION

The modal analysis was solved for the first 1,000 eigenmodes m of the structure, thus spanning a frequency range of up to 21 kHz. Table 5 provides an overview of a number of circumferential eigenmodes m and their respective natural frequencies f_{n} for two different cases: one considering only the stator lamination, and the other for the whole machine. The latter corresponds to those shown in Figure 6 for an element size of 5 mm. As can be seen from the results, the eigenfrequencies increase when additional components, such as the casing, are modelled in addition to the stator alone. Note that the subsequent analyses were not limited to circumferential modes only.

For the subsequent *harmonic response*, knowledge about the excitation frequencies and wave numbers at all operating points of interest is required. The investigated machine has

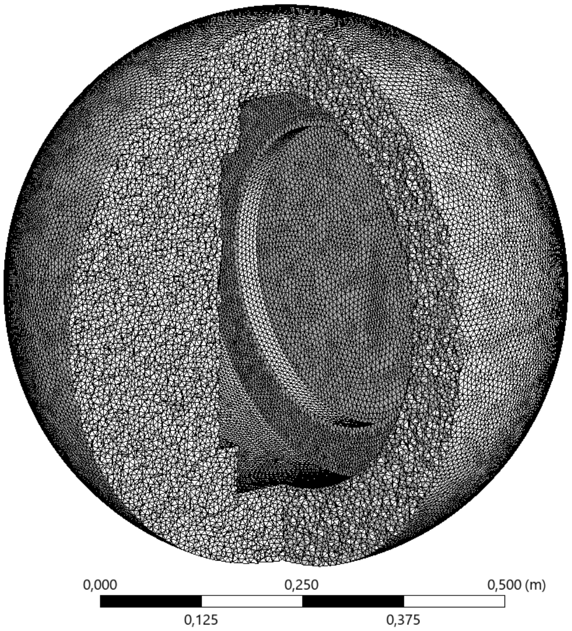

Figure 8. Meshed sphere with 3.1 million elements around the machine used for the *harmonic response* analysis of frequency band "1". The region inside the machine is not meshed in order to shorten the computational time. See Table 4 for reference.

20 poles or 10 pole-pairs. The electric frequency is a function of the rotational speed and is given by

$$f_{\mathrm{el}} = f_{\mathrm{m}} p, \tag{16}$$

where f_{m} is the mechanical frequency. At a speed of 6,000 rpm, which is the output shaft rotational speed of the Arriel 1E2 gas turbine installed on the EC145, the electric frequency is thus 1,000 Hz. This means that over the course of 1 ms, a north and a south pole pass a stator tooth. Due to the quadratic relationship between the force densities f_{r} and f_{t} and the magnetic flux densities B_{r} and B_{t}, the resulting force excitation occurs at twice the electric frequency and its even-numbered multiples, leading to certain time orders.

An electromagnetically excited force wave rotates inside the air gap and can be decomposed into a sum of sine waves, leading to certain excitation mode shapes (Ref. 20). These shapes have a spatial order (or spatial wave number) r and a distinct frequency or time order. A structural mode m can then be excited by a force wave with the same spatial order (or wave number) r. If the frequency of the force excitation is also close to the natural frequency of the structure, a resonance effect will occur, giving rise to increased noise radiation.

The spatial order of the first force wave component can be estimated as

$$r = \mathrm{GCD}(N/m_{\mathrm{ph}}, 2p). \tag{17}$$

Here, GCD is the greatest common divisor, and m_{ph} is the number of phases, which equals three in the current machine

Table 5. Eigenfrequencies f_{n} obtained from the modal analysis for the first circumferential eigenmodes m. Results for stator only and the whole structure considered.

	Eigenfrequency in Hz	
Mode	Stator only	Stator, casing, bearing and shaft
0	2,155	2,278
2	112	424
3	312	674
4	587	862
5	929	1,225
6	1,329	1,687
7	1,773	2,209
8	2,248	2,765

design. For the investigated machine, the first force wave component has a spatial wave number of $r = 4$. It occurs at twice the electrical frequency f_{el} of 2,000 Hz. Its electrical time order is therefore 2, while its mechanical time order is 20. The spatial order of the second force wave component is then $r = 2 \cdot \mathrm{GCD}(N/m_{\mathrm{ph}}, 2p) = 8$ at a frequency of 4,000 Hz, while the spatial order of the third force wave component is $r = 12$, occurring at a frequency of 6,000 Hz. Their mechanical time orders are thus 40 and 60, respectively.

The *harmonic response* was solved for a number of different rotational speeds across the continuous power-speed curve, shown in Figure 5. For each of the investigated speed points, the forces obtained by the electromagnetic simulation for this rotational speed were applied to the stator teeth. With the results of the *harmonic response*, the waterfall diagram in Figure 9 was created, showing the equivalent radiated power as a function of rotational speed and mechanical time order.

As can be deduced from the data, the first four mechanical time orders (20, 40, 60, and 80) are the dominant ones throughout the whole speed regime of the machine, with time order 20 being the most prominent one. At a rotational speed of 2,500 rpm, the maximum sound power level is reached at the mechanical time order 20, i.e., at a frequency of 833.3 Hz. At the operating point with a rotational speed of 6,000 rpm, the peak ERP level of 93.9 dB is found at the same time order and therefore at a frequency of 2,000 Hz.

While the waterfall diagram shows the ERP over the whole speed range of the machine, Figure 10 provides an impression of the ERP as well as the true radiated power as a function of frequency at a constant speed of 6,000 rpm. Additionally, the mechanical time order is given. At this operating point, the machine will provide its maximum continuous power. As previously mentioned, excitation occurs at even-numbered multiples of the electrical frequency. The highest ERP level is found at 2,000 Hz. Between 4,000 and 8,000 Hz, values in the range of 72 to 77 dB are observed. Starting at 10 kHz and above, the levels fall below 50 dB. The Helmholtz number for an excitation frequency of 2,000 Hz, with a radius of the housing of the machine of 251.45 mm and a speed of sound of

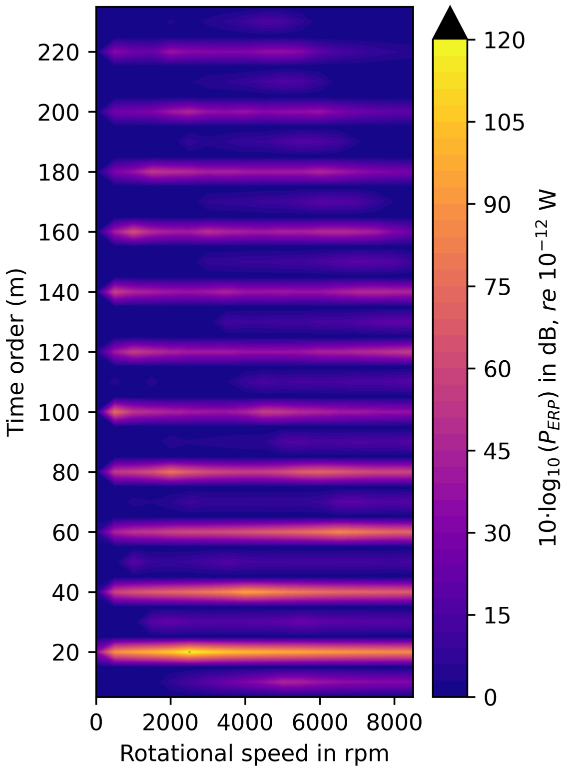

Figure 9. Equivalent radiated power of the machine as a function of speed and mechanical time order.

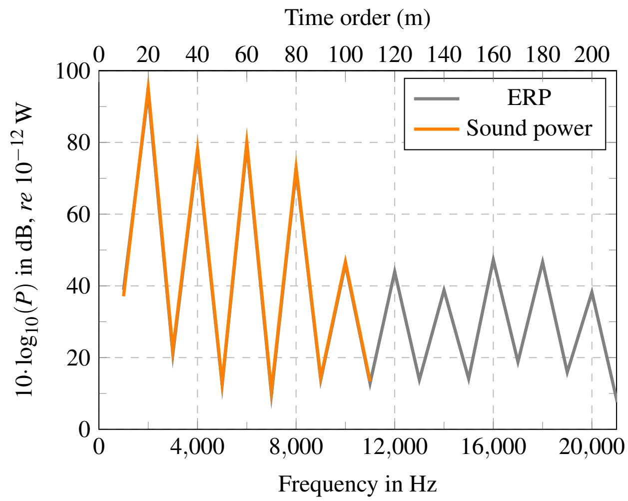

Figure 10. Equivalent radiated and sound power of the machine as a function of frequency for a constant rotational speed of 6,000 rpm.

340 m/s, equals 9.29, indicating high-frequency radiation. At higher excitation frequencies, the Helmholtz number will further increase. Thus, the ERP already gives reasonable results over the whole investigated frequency range when compared to the true radiated power. An overestimation of the ERP is not occurring for this machine at the investigated operating point.

While the previous results show that the noise estimation for the machine can be solely based on the coupled modal analysis and *harmonic response* approach, the *harmonics acoustic* analysis provides additional information that can be analysed and discussed, giving more insight into the details of the noise radiation.

Figure 11 shows the acoustic pressure (i.e. the local pressure deviation from the ambient atmospheric pressure) obtained from the latter for three different investigated frequencies, 2,000, 4,000 and 6,000 Hz, on a slice through the centre of the mass of the machine in the middle of the sphere. The result for the first frequency is taken from the model for frequency band "0", while the other two are taken from band "1". Therefore, the buffer layer around the housing and, consequently, the model extent is larger for the first one compared to the other two. The radial extent of the housing in all three pictures is kept the same, as is visible from the scales at the bottom of each picture.

As mentioned previously, the rotating force wave inside the air gap can be decomposed into a number of force wave components with certain spatial wave numbers r. At a frequency of 2,000 Hz, the dominant spatial wave number is four. It excites the stator teeth and, therefore, the attached structure. Its effect on the outer casing and thus on the local pressure is visible in Figure 11 (a). The acoustic pressure has four nodes of positive and four nodes of negative pressure originating from the housing surface and, by this, takes a distinct circumferential mode shape. The spiralling pattern indicates that it is a rotating sound source. It does so with a frequency equal to the excitation frequency. While the rotor of the machine and, therefore, the force wave in the air gap is rotating in a clockwise direction, the resulting source at the housing is rotating in an anti-clockwise direction.

At a frequency of 4,000 Hz, the dominant spatial wave number is eight, while at a frequency of 6,000 Hz it is twelve. The spiralling pattern is present at 4,000 Hz and, therefore, the source is rotating once again. The pattern for the last shown frequency is different from the previous ones. Here, the source appears to be standing. The deviation from the local to the ambient atmospheric pressure is lower for the last two frequencies compared to the first one.

The directivity of the radiated sound of the machine is shown in Figure 12. For each frequency at time orders 20, 40, and 60, the sound pressure level was obtained at 180 positions on a circle around the machine at a distance of 1 m. The circle starts at the front of the machine at an angle of θ of 0°. At the top of the machine, the angle is 90°, while it is 270° at the bottom. The obtained sound pressure level is different for the investigated frequencies. It has a symmetric shape, with the largest levels obtained at the top between 30 and 150° and at the bottom between 210 and 330°. In this direction, the sound pressure level is between 78.8 and 86.9 dB for a frequency of 2,000 Hz, between 39.7 and 73.2 dB for a frequency of 4,000 Hz, and between 52.7 and 80.2 dB for a frequency of 6,000 Hz. Starting at a frequency of 4,000 Hz, the directivity pattern exhibits additional lobes at intervals of 10 degrees,

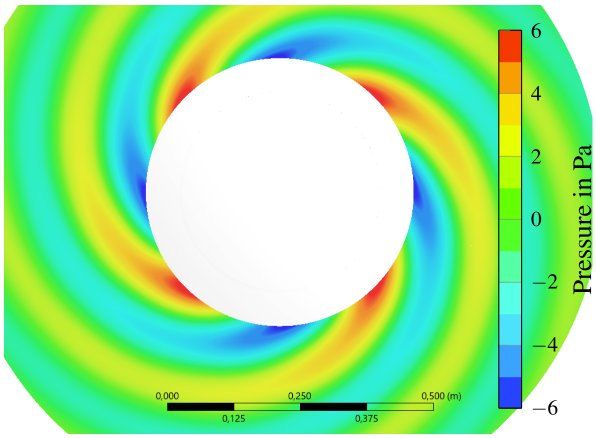

(a) 2,000 Hz, $r = 4$

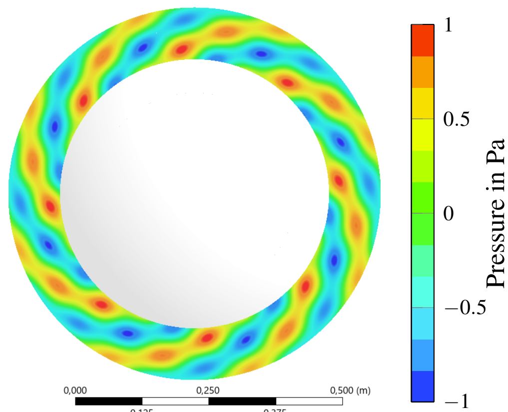

(b) 4,000 Hz, $r = 8$

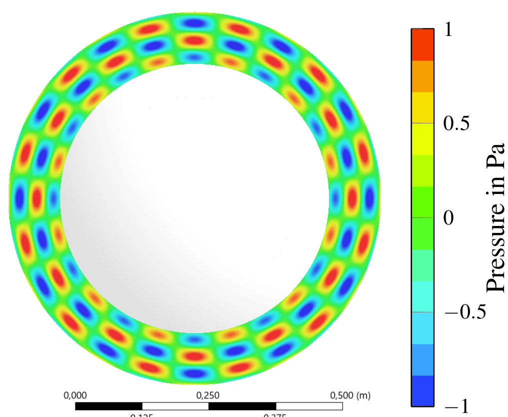

(c) 6,000 Hz, $r = 12$

Figure 11. Acoustic pressure inside the sphere around the machine for three excitation frequencies. The solution for 2,000 Hz is coming from a different frequency band, thus having a larger sphere extent.

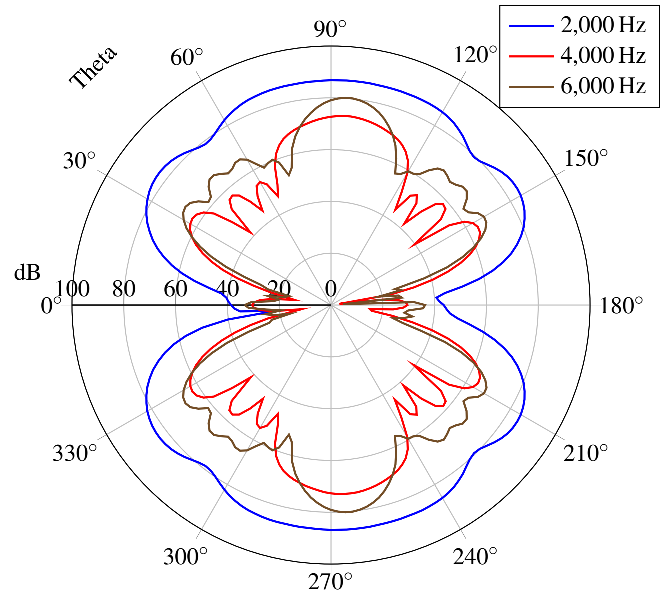

Figure 12. Directivity plot of the machine, showing the sound pressure level at a distance of 1,m around the machine for three excitation frequencies.

beginning at an angle θ of 30°. The sound levels are highest between 70 and 110°, which corresponds to the radial outward direction of the housing. Conversely, the sound pressure level is at its lowest in the axial direction of the machine, i.e., at 0 and 180 degrees.

CONCLUDING REMARKS

In this study the noise generated by an electric machine used as a supplementary power source during specific flight phases in a parallel hybrid powertrain was investigated. The investigation was conducted using simulation-based methods.

A workflow was developed to facilitate this analysis, encompassing the pre-design and subsequent optimization of the machine. The workflow incorporates both simplified and high-fidelity methods to estimate the radiated sound and its directivity pattern.

The paper outlines the following steps and analyses that were conducted:

1. A mission profile for an EC145 helicopter in an Emergency Medical Services (EMS) operation was obtained and prepared for further analysis.

2. Based on the mission profile, the required power for the helicopter was calculated for each flight phase, and the contribution of the electric machines in specific flight phases was determined.

3. The mass of necessary components was estimated.

4. An electric machine was designed and optimized in a subsequent step based on the obtained power rating.

5. A modal analysis combined with a harmonic response analysis was conducted to determine the equivalent radiated power at specific time or motor orders.

6. Through multiple harmonic acoustic simulations, the directivity of the machine and the acoustic pressure field around it were obtained, revealing distinct patterns linked to the exciting force wave inside the air gap.

7. Additionally, a comparison between the simplified harmonic response approach and the higher-fidelity harmonic acoustic approach was performed, indicating that the simplified method yields qualitatively sufficient results.

The analysis yielded estimated sound power levels in the range of 73 to 95 dB across a frequency spectrum of up to 8,000 Hz. Furthermore, sound power levels of up to 87 dB were measured at a distance of 1 m in the normal direction of the enclosing housing. The highest levels were observed at lower motor or mechanical time orders, indicating a correlation between the sound source and the electromagnetically induced forces within the air gap. These forces are a function of the magnetic field of the armature and the permanent magnets.

The results of this study suggest that the noise generated by electric machines constitutes a significant noise source that warrants consideration during the design phase of future parallel hybrid propulsion systems for helicopters.

It is noted that the simplified geometries employed for the housing, shaft, and bearings may influence the results. Moreover, the integration of the electric machine's rotor with the gas turbine shaft and the incorporation of the housing into the helicopter's structure may lead to integration effects, including alterations in eigenfrequencies, altered radiation surfaces, and potential shielding effects. These effects were not accounted for in the present analysis to maintain simplicity.

Author contact:
Sebastian Hakansson, sebastian.hakansson@dlr.de

ACKNOWLEDGMENTS

The author thanks Enrico Teichert for performing the optimization workflow on the initial design, Frederik Heise for designing the cooling concept for the machine and Thomas Geyer as well as Erik Schneehagen for their help with the manuscript. All four are part of the Institute of Electrified Aero Engines of the German Aerospace Center.

REFERENCES

1. P. Jänker, J. Stuhlberger, F. Hoffmann, G. Niesl, and V. Kloeppel. The hybrid helicopter drive - A step to new horizons of efficiency and flexibility. In *36th European Rotorcraft Forum*, 2010.

2. C. Sanabria-Walter. Design of a 600 kW ring-type direct-drive Flux-Switching Permanent Magnet machine for aerospace main propulsion. In *2014 16th European Conference on Power Electronics and Applications*, pages 1–10. IEEE, 2014. doi:10.1109/EPE.2014.6910781.

3. C. Mercier and M. Gazzino. State of the art of Helicopter Hybrid Propulsion. In *Proceedings of the 72nd AHS International's Annual Forum & Technology Display (AHS Forum 72)*, 2015. doi:10.4050/F-0072-2016-11519.

4. I. Bolvashenkov, J. Kammermann, and H.-G. Herzog. Electrification of helicopter: Actual feasibility and prospects. In *13th IEEE Vehicle Power and Propulsion Conference (VPPC'17)*, pages 1–6. IEEE, 2017. doi:10.1109/VPPC.2017.8330883.

5. D. Filusch, M. Breiteneder, and H.-G. Herzog. Design of a Hyperconducting Synchronous Machine for High-Torque Applications. In *2018 XIII International Conference on Electrical Machines (ICEM)*, pages 2092–2098. IEEE, 2018. doi:10.1109/ICELMACH.2018.8506697.

6. D. Filusch, J. Zucker, and H.-G. Herzog. A Novel Hydrogen-Based Thermal Management System for an Electric Helicopter. In *2022 IEEE Vehicle Power and Propulsion Conference (VPPC)*, pages 1–7. IEEE, 2022. doi:10.1109/VPPC55846.2022.10003455.

7. P. Gonzalez, G. Buigues, and A. J. Mazon. Noise in electric motors: A comprehensive review. *Energies*, 16(14):5311, 2023. doi:10.3390/en16145311.

8. B. Zaghari, A. Kiran, T. Sinnige, E. Pontika, H. B. Enalou, T. Kipouros, and P. Laskaridis. The impact of electric machine and propeller coupling design on electrified aircraft noise and performance. In *AIAA SciTech 2023 Forum*, page 2133, 2023. doi:10.2514/6.2023-2133.

9. I. Bolvashenkov, J. Kammermann, Z. Wenbin, I. Frenkel, and H.-G. Herzog. Comparative Reliability Analysis of Different Traction Drive Topologies for a Search-and-Rescue Helicopter. In *Stochastic Models In Reliability Engineering*, pages 331–354. CRC Press, 2020.

10. T. Donateo, A. Carlà, and G. Avanzini. Fuel consumption of rotorcrafts and potentiality for hybrid electric power systems. *Energy Conversion and Management*, 164:429–442, 2018. doi:10.1016/j.enconman.2018.03.016.

11. AirNav Radar. Flight tracking using AirNav Radar. https://www.airnavradar.com/. Accessed: 2024-07-30.

12. J. M. Seddon and S. Newman. *Basic Helicopter Aerodynamics, Second Edition*. Blackwell Science Ltd, 2001.

13. Z. Petrović, S. Stupar, I. Kostić, and A. Simonović. Determination of a Light Helicopter Flight Performance at the Preliminary Design Stage. *Journal of Mechanical Engineering/Strojniški Vestnik*, 56(9), 2010.

14. Eurocopter. Eurocopter: EC145 Technical Data. https://web.archive.org/web/20061111163435/http://www.eurocopter.com/ec145/TD_EC145.pdf. Accessed: 2024-05-29.

15. J. Kugener, A. Pal, and S. Kazula. Preliminary design tool for power converters in electric aircraft propulsion systems. In *Deutscher Luft- und Raumfahrtkongress (DLRK)*, 2024. doi:10.25967/610355.

16. J. Kugener and S. Kazula. Preliminary design and evaluation of inverter power density and reliability in electric aircraft propulsion systems. In *PCIM Europe 2024; International Exhibition and Conference for Power Electronics, Intelligent Motion, Renewable Energy and Energy Management*, pages 3313–3322. VDE, 2024. doi:10.30420/566262467.

17. S. Sahoo, X. Zhao, and K. Kyprianidis. A review of concepts, benefits, and challenges for future electrical propulsion-based aircraft. *Aerospace*, 7(4):44, 2020. doi:10.3390/aerospace7040044.

18. S. Kalt, J. Erhard, and M. Lienkamp. Electric machine design tool for permanent magnet synchronous machines and induction machines. *Machines*, 8(1):15, 2020. doi:10.3390/machines8010015.

19. E. Teichert and S. Kazula. Overview and Evaluation of Electric Machines for Electric Regional Aircraft Propulsion Systems. In *Deutscher Luft- und Raumfahrtkongress*, 2024. doi:10.25967/630118.

20. S. Hakansson and T. Geyer. Untersuchung der Schallentstehung und -abstrahlung elektrischer Maschinen für neuartige elektrifizierte Luftfahrtantriebe. In *50. Jahrestagung für Akustik - DAGA 2024*, Fortschritte der Akustik, pages 569–572. Deutsche Gesellschaft für Akustik e.V., 2024. URL: https://elib.dlr.de/204144/.

21. K. Kvist, S. V. Sorokin, and J. B. Larsen. Radiation efficiency varying equivalent radiated power. *The Journal of the Acoustical Society of America*, 157(1):169–177, 2025. doi:10.1121/10.0034838.